Metall. Res. Technol. **123**, 216 (2026)

https://doi.org/10.1051/metal/2026009

Metallurgical Research & Technology

Available online at:
www.metallurgical-research.org

Special Issue on 'Innovations in Iron and Steelmaking', edited by Carlo Mapelli and Davide Mombelli

ORIGINAL ARTICLE OPEN ACCESS

Influence of alloying elements and strain rate on the second ductility minimum of microalloyed steels during simulated continuous casting

Saeid Bakhtiari[1,2,*], Saham S. Sharifi[2], Iman Sedighi[2], Sergiu Ilie[3], and Christof Sommitsch[2]

[1] K1-MET GmbH, Stahlstrasse 14, 4020 Linz, Austria
[2] Institute of Materials Science, Joining and Forming at the Graz University of Technology, Kopernikusgasse 24/I, 8010 Graz, Austria
[3] Voestalpine Stahl GmbH, voestalpine-Strasse 1, 4020 Linz, Austria

Received: 19 August 2025 / Accepted: 3 January 2026

Abstract. The ductility behavior of continuously cast steel is a key factor influencing strand quality and crack susceptibility. Therefore, investigating the parameters that affect ductility is of great importance for enhancing the productivity of the method by producing defect-free products. This study investigates the differences in ductility behavior between two microalloyed steels with different C, Mn, Al, Ti, B, and S content subjected to hot tensile testing at strain rates of $10^{-2}\,s^{-1}$ and $10^{-3}\,s^{-1}$ at 750 °C, 800 °C, and 850 °C. The first material is low-carbon microalloyed steel with a higher amount of Mn, Al, and S, and the second contains higher C, Ti, and B. Both steels were tested after in-situ melting using an induction heating system in a vacuum chamber, followed by a hot tensile test until fracture. An initial microstructural analysis was conducted to study the influence of chemical composition, temperature, and strain rate on both steels. Furthermore, the precipitation kinetics of both steels were evaluated using MatCalc software, which provided predictions for the expected precipitates. The results indicate that the steel with higher C, Ti, and B, and lower Mn and S content exhibits better ductility at both strain rates. This was attributed to the influence of alloying elements on the formation of precipitates and the kinetics of austenite-ferrite transformation, in addition to fewer MnS particles. These effects are associated with the preferential formation of coarse TiN rather than AlN and BN.

Keywords: hot ductility / continuous casting / ductility minimum / micro-alloyed / strain rate / steel

1 Introduction

Due to its high efficiency, large production capacity, and low energy consumption, continuous casting is the primary method of steel making with approximately 96.7% of total steel production [1,2]. Emerging from the mold during continuous casting, the strand encounters multiple forces, including ferrostatic pressure, roll compression, bulging, thermal expansion, and tension. The outcome of these multiple forces, particularly after bending and straightening, is tensile stress, which can lead to various internal and surface defects [3–5]. Among these defects, the transverse corner crack, examined in this study, can form within the specific temperature range where the ductility of the strand is insufficient to withstand the applied stress, known as the second ductility minimum [3,5,6]. The study of the ductility behavior of steel is a key factor in understanding and controlling crack formation during continuous casting, thereby reducing production cost. To measure the ductility of the strand on a laboratory scale, the reduction of area (RA) values of the hot tensile test samples deformed until fracture must be calculated. To achieve reliable results, the test condition must resemble the industrial process. Therefore, it is recommended to apply the solution treatment at 1350 °C and perform the tensile test at a strain rate of $10^{-3}\,s^{-1}$ [7,8].

The ductility of steels during the continuous casting process is affected by their chemical composition and thermomechanical conditions. The second ductility minimum, typically observed between 700 °C and 1000 °C, is associated with the formation of ferrite along austenite grain boundaries and the precipitation of alloying elements. Both mechanisms are influenced by chemical composition and deformation conditions [9–12].

* e-mail: saeid.bakhtiari@k1-met.com

Table 1. Chemical composition of two steel grades measured by optical emission spectroscopy (OES).

Elements [wt.%]	Chemical composition									
	C	Cr	Mn	Al	Ti	B	Si	S	P	N
Steel 1	0.09	0.28	1.92	0.06	0.002	0.0003	0.15	0.005	0.009	0.005
Steel 2	0.27	0.33	1.21	0.03	0.027	0.0026	0.23	0.0007	0.010	0.006

Studies show that the presence of a thin ferrite layer at austenite grain boundaries reduces the ductility of steel [5,8]. Depending on the thickness and the phase fraction of ferrite, the second ductility minimum may shift to lower or higher temperatures [13]. Mintz reported that when a significant amount of ferrite (approximately 45%) is formed, the ductility recovers, specifically at the low-temperature end of the ductility trough [7]. He showed that the extent of the trough is influenced by the deformability of ferrite films. During deformation, strain localizes in ferrite as the softer phase compared to austenite, leading to reduced ductility and promoting intergranular failure [5,7,8,14–17].

Microalloying elements are added to steel to achieve specific properties, for instance, hardness, deformability, and corrosion resistance. The addition of some alloying elements can improve the ductility behavior of the strand during continuous casting by suppressing the formation of the ductility trough [10,18–20]. Adding Ti improves the impact properties of the steel, and B is usually added to low-carbon steels to increase the hardenability [21–23]. The addition of both elements affects ductility behavior depending on their concentrations, as they influence the austenite-to-ferrite transformation temperature and the precipitation characteristics [8,18]. Ti is a strong nitride former; hence, it is reported that an addition of 0.02–0.04% Ti is beneficial for the ductility by consuming N and forming the coarse TiN [8,23–27]. By consuming N, B segregates at the grain boundaries and strengthens them. The B atoms occupying vacancies at the grain boundaries prevent the formation and propagation of microcracks. Moreover, B segregation retards the formation of pre-eutectoid ferrite at grain boundaries, thereby delaying crack initiation [12,28–33]. Furthermore, investigations show that an addition of 0.02–0.04%Al to high Mn steels (1.4%Mn) containing N (0.005%N) widens and deepens the ductility trough, indicating the reduction in ductility [5,8,24,34].

Strain rate is another key factor with a significant influence on the second ductility minimum. Strain rate can be translated to the deformation speed or casting velocity during the industrial process. The strain rate of $10^{-3}\,s^{-1}$ is usually used in hot ductility tests to simulate the straightening step in the continuous casting process [5,20,35,36]. An increase in strain rate has often been reported to improve the hot ductility of microalloyed steels, as demonstrated in the previous study and supported by much research [5,11,13,16,20,35,37,38].

Several studies have reported an improvement in ductility following the addition of B and Ti in steels [23,26,28,29]. The Influence of either Ti or B on hot ductility has been observed depending on testing conditions and N content in various studies [30–32]. However, research on hot ductility in continuously cast microalloyed steels considering simultaneously the amount of C, Ti, Al, S, Mn, and B is limited. Chemical composition changes the transformation kinetics, and hence, the deformability of the material. On the other hand, the synergistic influence of chemical composition—particularly the combined effects of C, Mn, Ti, Al, S, and B—is especially important, as the concurrent presence of these elements can significantly modify precipitation behavior [8,39,40]. However, there is still limited understanding on how the combined presence of C, Mn, Al, S, Ti, and B influences hot ductility, especially under conditions representative of continuous casting. The combined effects of these elements can change the phase transformation behavior and the precipitation processes that determine grain-boundary strength and the deformation response of the strand.

The present study investigates the combined influence of C, Mn, Al, S, Ti, and B on the hot ductility of two low-carbon steels under different deformation conditions. The investigation includes an evaluation of different strain rates and temperatures and the related microstructural changes that influence thermomechanical response. Hot tensile tests were performed to provide a closer representation of the conditions experienced during continuous casting. Phase transformations and precipitation behavior were characterized by using light optical microscopy (LOM) and scanning electron microscopy (SEM). In addition, MatCalc simulations were performed as a precipitate modelling tool to evaluate the precipitation behavior. The results were confirmed with experimental measurements using the energy-dispersive X-ray spectroscopy (EDX) technique.

2 Material and methods

Two microalloyed steel grades used in this work were provided by voestalpine Stahl GmbH. For a closer representative of industrial samples, the tensile samples were taken from the cast slab surface. The chemical composition of the two studied steels with different C, Ti, B, Mn, S, and Al content are listed in Table 1.

2.1 Hot ductility behavior

Cylindrical samples are cut in a way that their axes are aligned parallel to the casting direction. The samples are melted in situ in a thermomechanical simulator tensile testing machine, BETA 250-5, equipped with a vacuum chamber and an induction heating system, followed by solidification and hot tensile testing at 750 °C, 800 °C, and

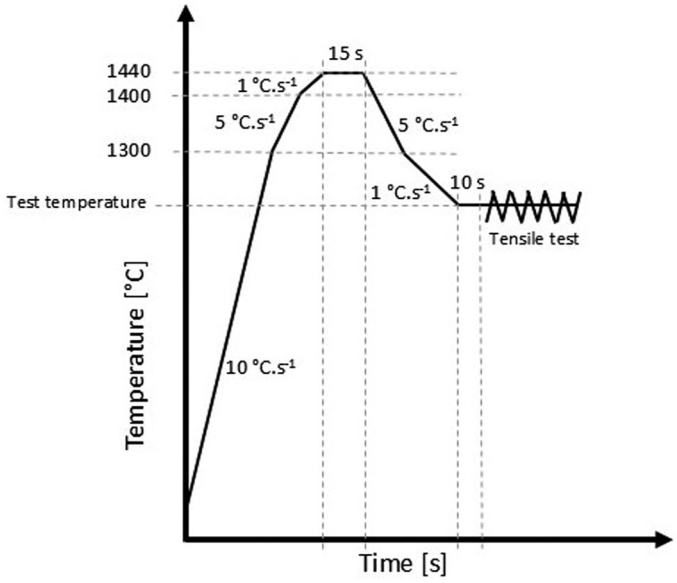

Fig. 1. Thermomechanical path of hot tensile test using BETA 250-5 [13].

850 °C, until fracture at two strain rates of 10^{-2} s^{-1} and 10^{-3} s^{-1}. The machine setup and the geometry of the samples are explained in detail in the previous work [13]. The samples were heated up to 1440 °C with three different heating rates (10 °C s^{-1} up to 1300 °C, 5 °C s^{-1} up to 1400 °C, and 1 °C s^{-1} up to 1440 °C) to have a proper control on the temperature in a way that the center of the sample melted, while the thin oxide-covered layer of the steel remained solid to prevent the molten material from spilling out. This method provides the closest condition to the industrial casting and represents the strand emerging from the mold. To measure the temperature, a pair of S-type thermocouples was welded to the surface of the sample at its midpoint. After 15 seconds of soaking time, the samples cooled down to 1300 °C at a cooling rate of 5 °C s^{-1}. To have a better understanding of the initial microstructure of the samples after melting and solidification, at this stage, the grain sizes of the equiaxed grains of steel 1 and steel 2 are measured 200 μm and 260 μm, respectively, in accordance with the ASTM E112. Then, cooling the samples continues down to the test temperature by 1 °C s^{-1}. The samples were held at the test temperature for 10 seconds before the start of the test (Fig. 1). This thermomechanical path was chosen because it allows appropriate control during the heating step and represents the industrial casting condition during the cooling step.

The ductility curves are obtained by plotting the reduction of area of the hot tensile test specimens after fracture, calculated by Equation (1), against temperature for two different strain rates.

$$\%\,RA = \left(\frac{A_0 - A_f}{A_0}\right) \times 100, \qquad (1)$$

Where RA, A_0, and A_f are the reduction of area, the initial cross-sectional area, and the measured surface area after fracture, respectively. Measuring the fracture surface was conducted by macro imaging using a stereo microscope, Zeiss Discovery.V20 (Carl Zeiss AG, Oberkochen, Germany). For microstructural analysis, an Axio Observer inverted LOM (Carl Zeiss AG, Oberkochen, Germany) was employed, and the samples for LOM imaging were etched with Nital 3%. To study the fracture mechanisms, the fracture surfaces of the samples were examined using TESCAN Mira3 field emission SEM (TESCAN, Dortmund, Germany) with an accelerating voltage of 15 kV.

2.2 Precipitation behavior

To investigate the precipitation behavior, thermokinetic simulations were carried out using MatCalc software (version 6.04/rel 1.005, MatCalc Engineering GmbH, Vienna, Austria). The simulations replicated the thermal cycle-including melting, cooling, and hot tensile testing-by applying the same parameters used in the laboratory experiments, such as test temperatures, cooling rate, and strain rate. MnS, AlN, and BN were considered in the simulations for steel 1, and MnS, BN, TiN, and $M_{23}C_6$ were considered for steel 2. For both steels, the simulations were carried out at three temperatures: 750 °C, 800 °C, and 850 °C. For steel 1, precipitation of AlN was considered at grain boundaries (GB), on the surface of MnS, and at the dislocations (Disl.). The rest of the particles were assumed to form on the grain boundaries and at the dislocations.

In the simulation setup, an effective volumetric misfit of 5% between MnS precipitates and the matrix is adopted, and no effective volumetric misfit is defined for AlN on the surface of MnS [41,42]. The simulation assumptions and results were validated through microscopy investigations of samples tested using the BETA 250-5 machine, as this experiment most closely replicates the continuous casting process. SEM combined with an Octane Super A C5 detector for the EDX was used for precipitates characterization. The measurements were conducted on samples from both steels tested at 750 °C and the strain rate of 10^{-3} s^{-1}. This condition was chosen because it gave a better comparison with the simulations.

3 Results

3.1 Hot ductility behavior

The RA values for the specimens deformed at temperatures of 750 °C, 800 °C, and 850 °C, and two strain rates of 10^{-2} s^{-1} and 10^{-3} s^{-1} are plotted in Figure 2. The horizontal dashed line represents the well-accepted threshold for transition from brittle to ductile fracture [17]. This curve depicts the ductility behavior of both steels under the selected test conditions.

The results indicate that, in general, by increasing the temperature, the ductility improves except for steel 1 at 800 °C, which has the lowest ductility at this temperature. For steel 1, the RA values at the strain rate of 10^{-3} s^{-1} indicate poor ductility, and the material exhibits brittle fracture within this temperature range. At this strain rate, all the temperatures fall within the ductility trough known as the second ductility minimum (RA lower than 40%).

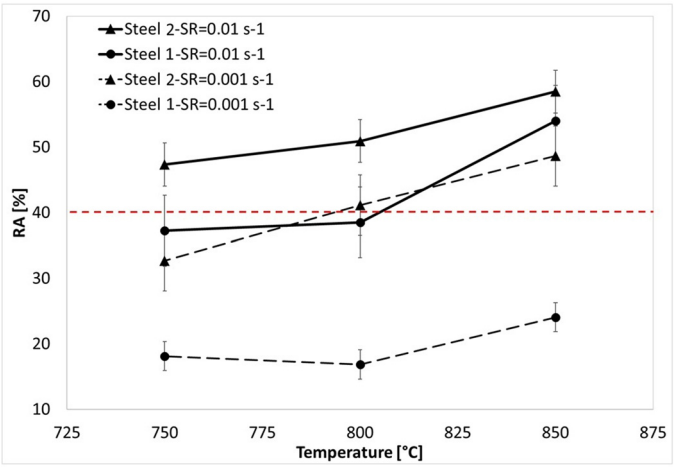

Fig. 2. Reduction of area under different thermomechanical conditions in steel 1 and steel 2.

At the higher strain rate, a transition from brittle fracture at 750 °C to ductile fracture at 850 °C is observed, indicating a recovery in ductility. In this case, ductility trough occurs at 750 °C and 800 °C. For steel 2, the transition from brittle fracture at 750 °C to ductile fracture at 850 °C occurs at the lower strain rate, i.e., 10^{-3} s^{-1}. At this strain rate, the ductility minimum is observed at 750 °C, while the ductility at 800 °C remains just above the critical threshold. At the higher strain rate, steel 2 exhibits ductile behavior throughout the entire temperature range, indicating low crack susceptibility. Comparing two materials, steel 2 shows better ductility under the tested conditions. Furthermore, as it is reported repeatedly [13,43], for both materials, the higher strain rate shows higher RA values, suggesting better ductility.

3.2 Microstructural observations

Figures 3 and 4 present the SEM images of the fracture surface for both steels deformed under different conditions. Fracture surfaces of steel 1 tested at the strain rate of 10^{-2} s^{-1} and at 750 °C show flat surfaces, indicating brittle fracture. The fracture surface showed sharp grain facets and intergranular fracture, with austenite grain surfaces covered by ferrite in steel 1 (Fig. 3a). As the temperature increases, dimples and voids appear on the fracture surfaces in steel 1, indicating a transition in fracture mechanism from brittle to ductile fracture (Figs. 3a–c). At 850 °C, the fracture surface is dominated by voids and dimples, indicating ductile fracture as the prevailing mechanism. In steel 2, the fracture surface at all tested temperatures is covered with dimples and voids, showing ductile fracture, with no evidence of intergranular fracture. The observations in both steels were consistent with the ductility curve shown in Figure 2.

At a lower strain rate, i.e., 10^{-3} s^{-1}, the fracture surface in steel 1 contains even fractured surfaces throughout the entire temperature range, translating to brittle fracture of these samples (Figs. 4a–c), as shown by the RA results. The fracture surface of steel 2 deformed at a slow deformation (10^{-3} s^{-1}) consists mostly of even surfaces and a small number of dimples-containing regions, as shown in Figure 4d. With increasing temperature, the area with dimples in the fracture surface of steel 2 increases, suggesting ductile fracture, as depicted in Figures 4d-f. These observations are consistent with the ductility curve shown in Figure 2.

Figure 5 shows the microstructure of both steels deformed at the strain rate of 10^{-2} s^{-1} at different temperatures. The LOM images reveal that, at 750 °C, thin ferrite films form along austenite grain boundaries in steel 1, Figure 5a, corresponding to the occurrence of intergranular fracture. The amount of ferrite decreases at 800 °C in steel 1, and no ferrite was detected at 850 °C, which correlates with improved ductility. This suggests that the presence of thin ferrite films at austenite grain boundaries plays a key role, causing a ductility trough. In contrast, steel 2 shows no ferrite formation at any tested temperature and demonstrates ductile fracture behavior in this temperature range.

The amount of ferrite increased with decreasing the deformation rate due to the prolonged time for ferrite nucleation Figures 6a–c. At the ductility trough, ferrite layers form along austenite grain boundaries. At 800 °C, these ferrite films were thinner than those at 750 °C. Thinner ferrite is more detrimental to ductility because it still creates a continuous brittle network along the grain boundaries but lacks enough thickness to accommodate train and deform plastically. Although less ferrite forms at 850 °C in steel 1, its negative effect is reduced since not all the austenite grain boundaries are covered by ferrite. Therefore, the ductility slightly improves at this temperature (Fig. 6c and Fig. 2). In steel 2, a small amount of deformation-induced ferrite forms at austenite grain boundaries at 750 °C and 800 °C, reducing the ductility compared to 850 °C, where no ferrite is present because the temperature exceeds the transformation point (Figs. 6d–f).

3.3 Precipitation behavior

3.3.1 Simulation results

Precipitation behavior was investigated through simulation and experimental measurements. The simulations were carried out using the software package MatCalc with various parameters to address both the size and phase volume fraction of precipitates. Table 2 and Table 3 list the type, the size, and the phase volume fraction of the precipitates present in both studied steels under two strain rates of 10^{-2} s^{-1} and 10^{-3} s^{-1}.

In general, the size and volume fraction of precipitates in both steels were not influenced by temperature and strain rate. Some variations are visible, specifically for MnS particles, yet due to a very low phase fraction, significantly fine particle size, and scattered distribution of these variations, they can be considered negligible. The results show that steel 1 contains larger MnS particles (approximately 10x) with a higher phase volume fraction (approximately 10000x), especially on the dislocations. The simulated results show a very trivial amount of MnS particles in steel 2. On the other hand, the size of precipitates in steel 2, i.e., TiN within the matrix, was

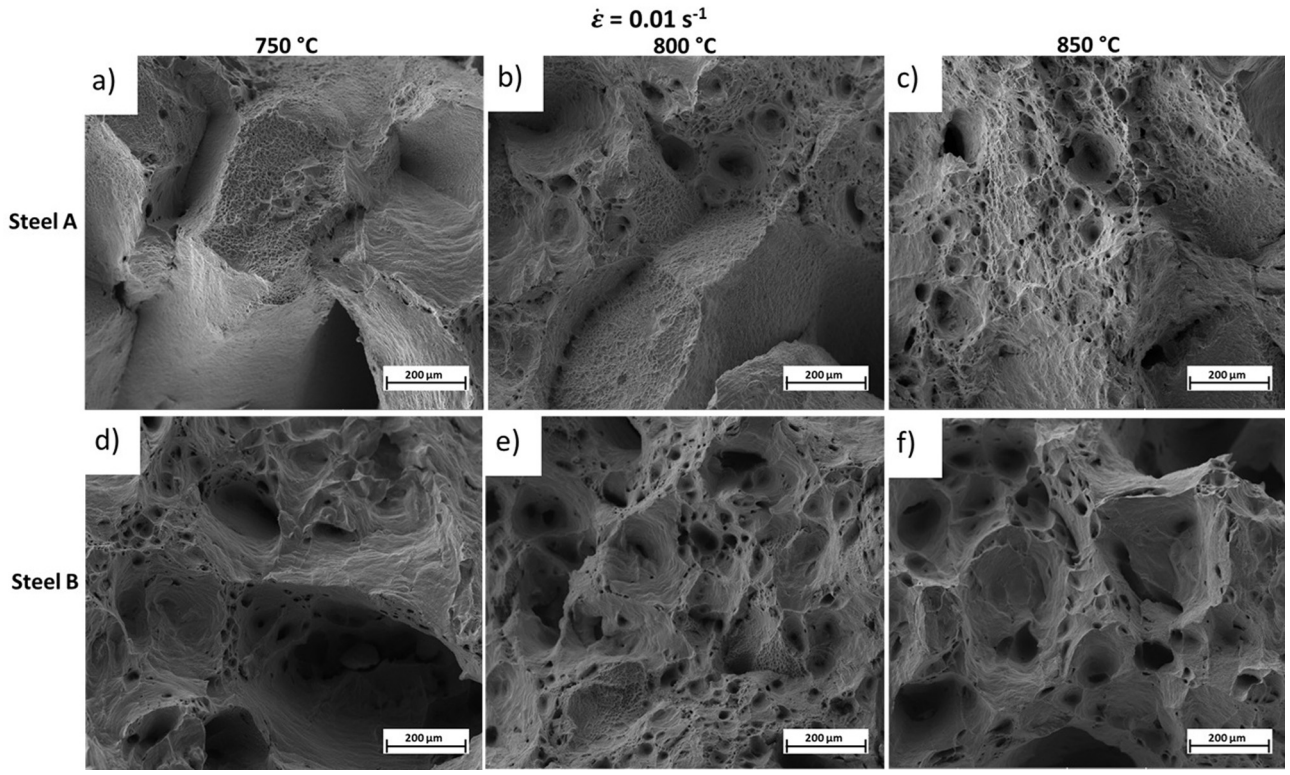

Fig. 3. SEM images of fracture surface of the hot tensile test samples at strain rate of 10^{-2} s^{-1} for steel 1: a) 750 °C; b) 800 °C; c) 850 °C and steel 2; d) 750 °C; e) 800 °C; f) 850 °C. The scale bar represents 200 µm.

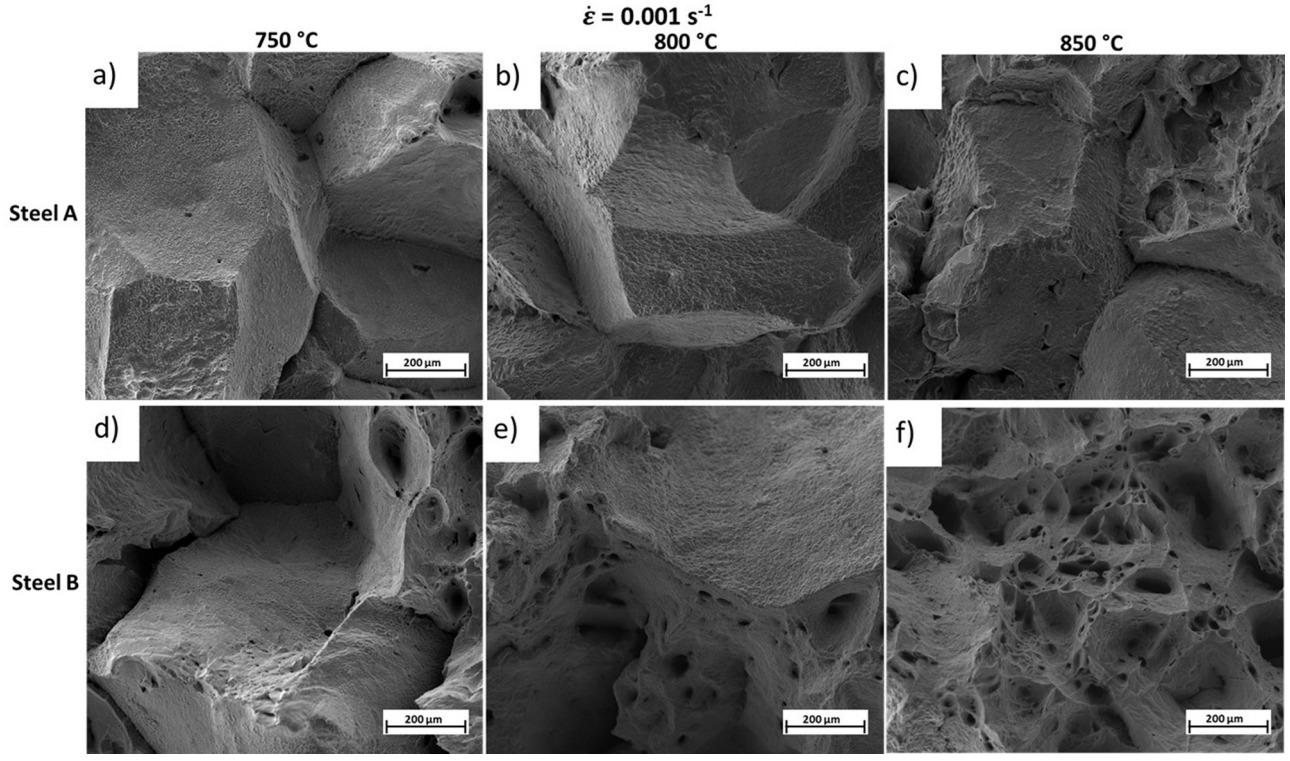

Fig. 4. SEM images of fracture surface of the hot tensile test samples at strain rate of 10^{-3} s^{-1} for steel 1: a) 750 °C; b) 800 °C; c) 850 °C and steel 2; d) 750 °C; e) 800 °C; f) 850 °C. The scale bar represents 200 µm.

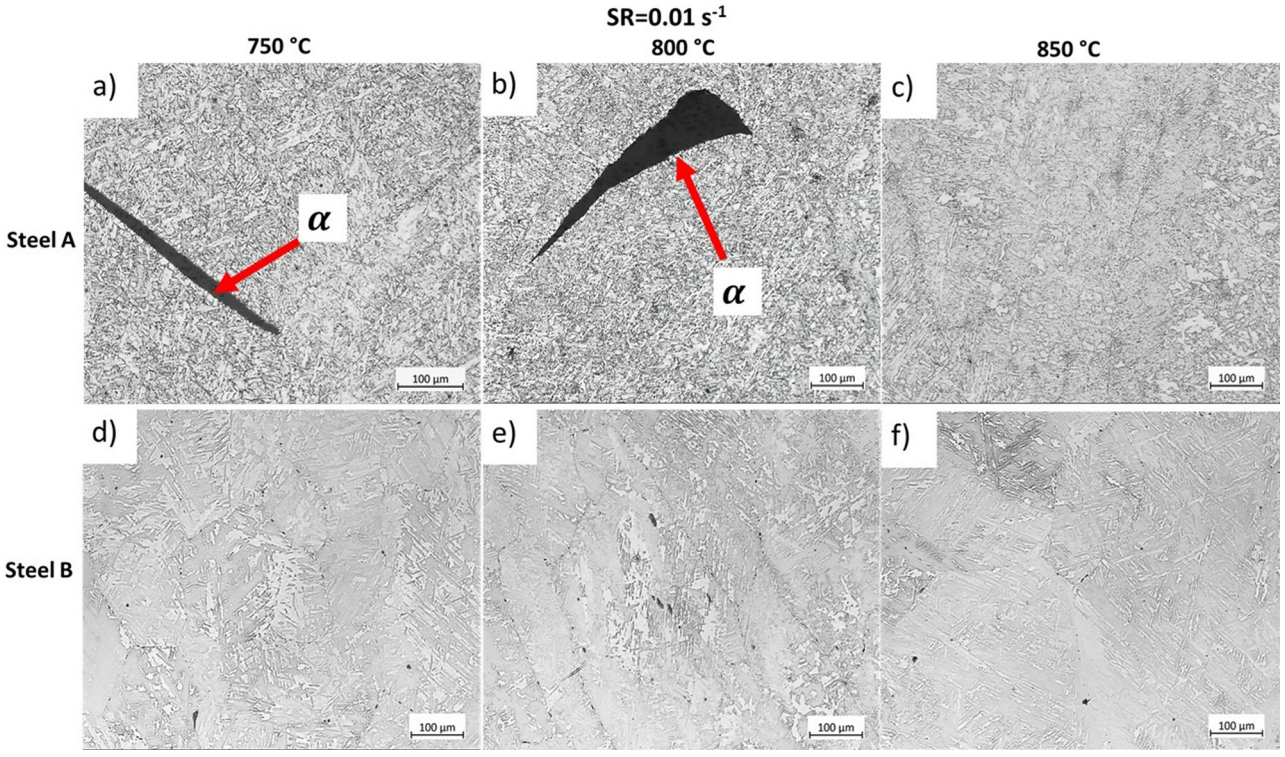

Fig. 5. LOM images of the hot tensile test samples at strain rate of 10^{-2} s^{-1} for steel 1: a) 750 °C; b) 800 °C; c) 850 °C and steel 2; d) 750 °C; e) 800 °C; f) 850 °C. The scale bar represents 100 µm.

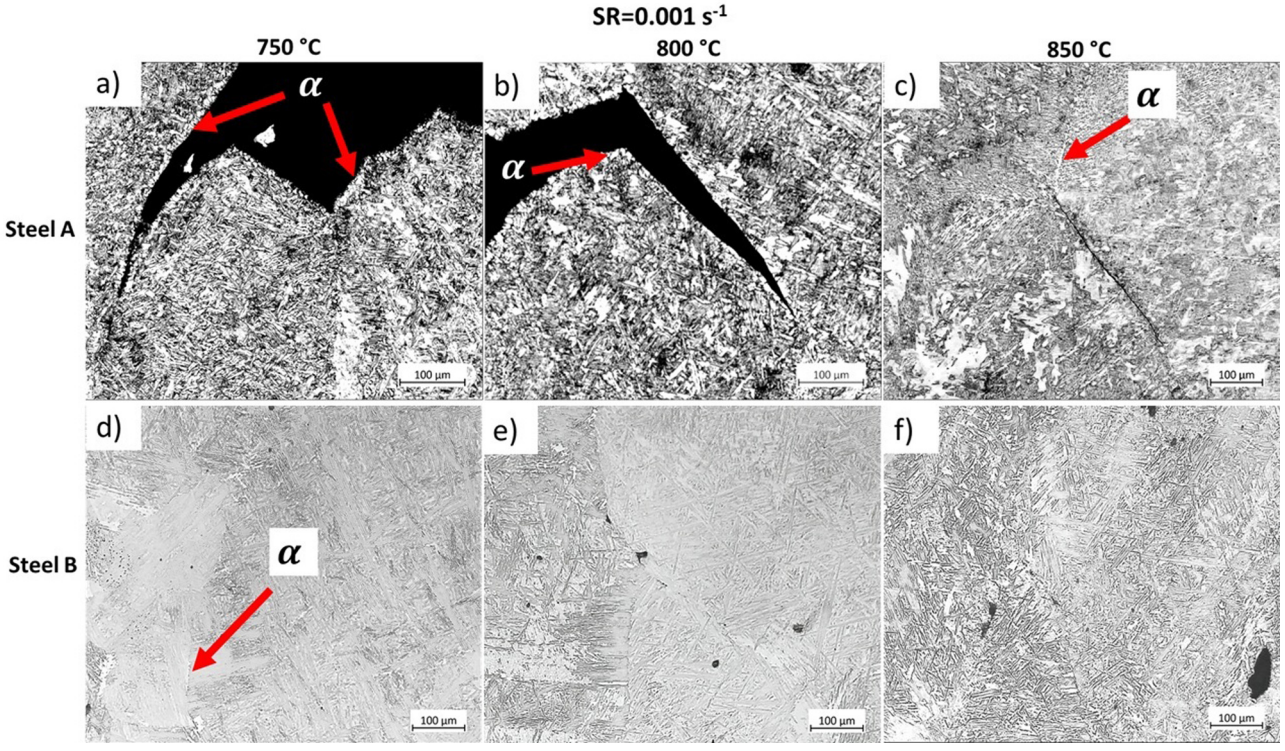

Fig. 6. LOM images of the hot tensile test samples at strain rate of 10^{-3} s^{-1} for steel 1: a) 750 °C; b) 800 °C; c) 850 °C [13] and steel 2; d) 750 °C; e) 800 °C; f) 850 °C. The scale bar represents 100 µm.

Table 2. Simulated results for the mean radius of precipitates in steel 1 and steel 2.

Mean radius (nm)		750 °C		800 °C		850 °C	
		10^{-2} s^{-1}	10^{-3} s^{-1}	10^{-2} s^{-1}	10^{-3} s^{-1}	10^{-2} s^{-1}	10^{-3} s^{-1}
Steel 1							
MnS	GB	196	197	196	197	196	197
	Disl.	8.8	9.2	8.8	10	8.7	14
AlN	GB	73	72	73	73	73	75
	Disl.	2.1	2.3	2.1	2.7	2.1	4.1
	MnS	2.2	2.3	2.2	2.8	2.2	4.1
BN	GB	208	285	208	285	208	285
	Disl.	0.5	0.6	0.5	0.6	0.5	0.6
Steel 2							
MnS	GB	19	24	18	28	18	37
	Disl.	0.5	0.5	0.5	0.5	0.5	0.5
TiN	GB	147	147	147	147	147	150
	Disl.	32	32	32	32	32	32
BN	GB	1449	1449	1449	1452	1448	1453
	Disl.	1.4	11	3	1.3	3.4	0.7
$M_{23}C_6$	GB	6.8	6.4	7.7	7.6	7.7	6.7
	Disl.	0.6	0.6	0.6	0.6	0.6	0.6

approximately 15x larger than precipitates in steel 1 (AlN) over all conditions. In both steels, the fraction of precipitates in the matrix was higher than the fraction of precipitates at the grain boundaries. Simulation results showed a very low phase fraction of $M_{23}C_6$ in steel 2. Therefore, this precipitate is not considered in the analysis.

3.3.2 EDX measurements

EDX analysis confirmed the presence of MnS and AlN in steel 1. Figure 7a and 7b show an isolated MnS particle and an AlN particle located on MnS, respectively. No free AlN particles were detected in steel 1 within the matrix.

Figure 8 presents the EXD measurements of steel 2. The measurements in steel 2 confirmed the presence of TiN precipitates, as predicted by MatCalc simulations. The size of TiN precipitates ranged from 150 to 250 nm, which is consistent with the simulation results. Due to the low atomic mass of B, the detection of BN precipitates by EDX was difficult, as also reported by another research group [44]. In addition to TiN, some Al/Ca and Al/Mg phases were detected.

4 Results and discussion

In this work, several factors that influence the hot ductility behavior of the microalloyed steels were studied. The most general observation in this study is that steel 2 showed better overall ductility than steel 1, as illustrated in Figure 2. The reasons behind this difference are discussed in the following section.

As shown in Figure 2, the deformation conditions have a clear influence on the hot ductility of both steels, which is consistent with previous studies [7,8,13,37,43]. The impact of the deformation conditions is commonly linked to three key mechanisms described in the literature: phase transformation, i.e., the development of deformation-induced ferrite and ferrite films along austenite grain boundaries, the nucleation and growth of precipitates, and the formation, coalescence, and growth of microvoids [7,8,16,39,43,45].

4.1 Deformation conditions

Faster deformation improves ductility. At a low strain rate, limited time is available for precipitate formation, crack initiation, and crack growth, which reduces the chances of intergranular failure. In addition, slower deformation promotes the formation of deformation-induced ferrite, which is softer than austenite and concentrates strain along grain boundaries and failure of the material. Moreover, slower strain rates promote dynamic recovery (DRV) of ferrite, which softens this phase and facilitates crack formation. On the other hand, faster deformation causes work hardening in ferrite and reduces its strain concentration [46].

Furthermore, both steels exhibit low ductility at lower temperatures. As the temperature decreases, undercooling increases, which provides the driving force for austenite to ferrite phase transformation. The formation of ferrite promotes strain localization, creating regions of stress concentration that facilitate crack initiation. Steel 2 showed better ductility than steel 1 over the tested conditions (see Fig. 2).

Table 3. Simulated results for the phase fraction of precipitates in steel 1 and steel 2.

Phase fraction		750 °C		800 °C		850 °C	
		10^{-2} s^{-1}	10^{-3} s^{-1}	10^{-2} s^{-1}	10^{-3} s^{-1}	10^{-2} s^{-1}	10^{-3} s^{-1}
Steel 1							
MnS	GB	9.1×10^{-9}	9.2×10^{-9}	9.1×10^{-9}	9.2×10^{-9}	9.1×10^{-9}	9.3×10^{-9}
	Disl.	2.5×10^{-5}	2.9×10^{-5}	2.6×10^{-5}	4.1×10^{-5}	2.6×10^{-5}	9.9×10^{-5}
AlN	GB	3.2×10^{-9}	3.2×10^{-9}	3.3×10^{-9}	3.2×10^{-9}	3.3×10^{-9}	3.3×10^{-9}
	Disl.	1.7×10^{-6}	1.9×10^{-6}	1.5×10^{-6}	2.9×10^{-6}	1.4×10^{-6}	9.5×10^{-6}
	MnS	1.7×10^{-7}	2.2×10^{-7}	1.8×10^{-7}	3.1×10^{-7}	1.7×10^{-7}	1.2×10^{-6}
BN	GB	1.4×10^{-9}	7.1×10^{-9}	1.4×10^{-9}	7.1×10^{-9}	1.4×10^{-9}	7.1×10^{-9}
	Disl.	3.1×10^{-5}	3.1×10^{-5}	3.1×10^{-5}	3.1×10^{-5}	3.1×10^{-5}	3.1×10^{-5}
Steel 2							
MnS	GB	9.3×10^{-11}	1.2×10^{-10}	9.3×10^{-11}	1.2×10^{-10}	9.3×10^{-11}	1.8×10^{-10}
	Disl.	1.3×10^{-9}	1.3×10^{-9}	1.3×10^{-9}	1.3×10^{-9}	1.3×10^{-9}	1.3×10^{-9}
TiN	GB	5.9×10^{-9}	6×10^{-9}	5.9×10^{-9}	6×10^{-9}	5.9×10^{-9}	6×10^{-9}
	Disl.	2.6×10^{-4}	2.6×10^{-4}	2.6×10^{-4}	2.6×10^{-4}	2.6×10^{-4}	2.7×10^{-4}
BN	GB	9.1×10^{-8}	9.1×10^{-8}	9.1×10^{-8}	9.1×10^{-8}	9.1×10^{-8}	9.2×10^{-8}
	Disl.	2.2×10^{-4}	2.2×10^{-4}	2.1×10^{-4}	2.2×10^{-4}	2.1×10^{-4}	2.2×10^{-4}
$M_{23}C_6$	GB	4.9×10^{-10}	4.1×10^{-10}	6.3×10^{-10}	5.0×10^{-10}	8.6×10^{-10}	4.2×10^{-10}
	Disl.	6.6×10^{-12}	2.6×10^{-12}	1.3×10^{-11}	6.9×10^{-12}	5.3×10^{-12}	4.8×10^{-13}

Figures 3a–c and 4a–c show the SEM images of steel 1 at different temperatures and the strain rates of 10^{-2} s^{-1} and 10^{-3} s^{-1}, respectively. Under a faster deformation, i.e., 10^{-2} s^{-1}, the micrographs consist of a mixture of flat fracture surfaces and dimples, indicating intergranular brittle fracture and ductile fracture, respectively, as shown in Figure 3a-c. On the contrary, at a slower deformation, the microstructure of the same material, steel 1, consists only of even brittle fracture surfaces with no ductile fracture characteristics, as shown in Figure 4a–c.

Figures 5 and 6 present the LOM images of both steels deformed under various thermomechanical conditions. For a given strain rate, the fraction of ferrite in steel 1 increases as the temperature decreases. For instance, in Figure 5c (at a strain rate of 10^{-2} s^{-1}), no ferrite was observed, whereas in Figure 5a, ferrite films are visible along the austenite grain boundaries (indicated by red arrows). A similar trend is observed when comparing Figures 6c and Figure 6a at a strain rate of 10^{-3} s^{-1}. Across the tested temperature range, no ferrite was detected in steel 2, except a trivial amount of ferrite at the lowest temperature due to enhanced undercooling. The reduced amount of ferrite in steel 2 compared to steel 1 is also attributed to the influence of alloying elements in steel 2, which impacts the phase transformation behavior of the steels.

4.2 Phase-transformation behavior

The transformation of austenite to ferrite affects hot ductility in both steels. Furthermore, the higher carbon content in steel 2 hinders the formation of ferrite and stabilizes austenite and decreases the transformation temperature, thereby reducing crack susceptibility caused by thin ferrite films at austenite grain boundaries [39]. On the one hand, B segregates at grain boundaries and retards the transformation of austenite to ferrite [8,12,32,33,47]. In this study, the segregation of elements is not examined. However, microstructural observations show that steel 2 contains less ferrite than steel 1, which indirectly supports the idea that B contributes to stabilizing austenite. In addition, MatCalc simulations indicate that the formation of BN at grain boundaries is negligible, with a mean radius of approximately 1450 nm and a volume fraction of approximately 10^{-7}. This suggests that BN does not form at the grain boundaries in steel 2 because Ti consumes the available N. As a result, B remains available and could segregate at grain boundaries, helping to delay ferrite formation and improve ductility.

4.3 Precipitation behavior

Higher ductility in steel 2 compared to steel 1 is associated with the behavior of precipitates. During the austenite to ferrite transformation, AlN tends to precipitate preferentially within the ferrite phase, increasing stress concentration and reducing ductility. Moreover, AlN precipitates can pin the grain boundaries and hinder their migration during deformation, which leads to crack initiation along these boundaries [5,8]. Additionally, higher Mn and S content in steel 1 encourages the formation of MnS inclusions that tend to precipitate during cooling. The presence of MnS promotes intergranular voiding, acts as nucleation site for deformation induced ferrite, and reduces ductility. As Table 2 and Table 3 show, the size and phase fraction of MnS particles in steel 1 are greater than that of steel 2 (10x and 10000x, respectively).

In steel 2, on the contrary, the amount of Al is too low (0.02–0.04 wt.%) to form AlN [8]. This contributes to the improved ductility of this steel compared to steel 1. Furthermore, the presence of Ti, as a strong nitride former, in steel 2, encourages the formation of TiN, which consumes available N and thereby suppresses the

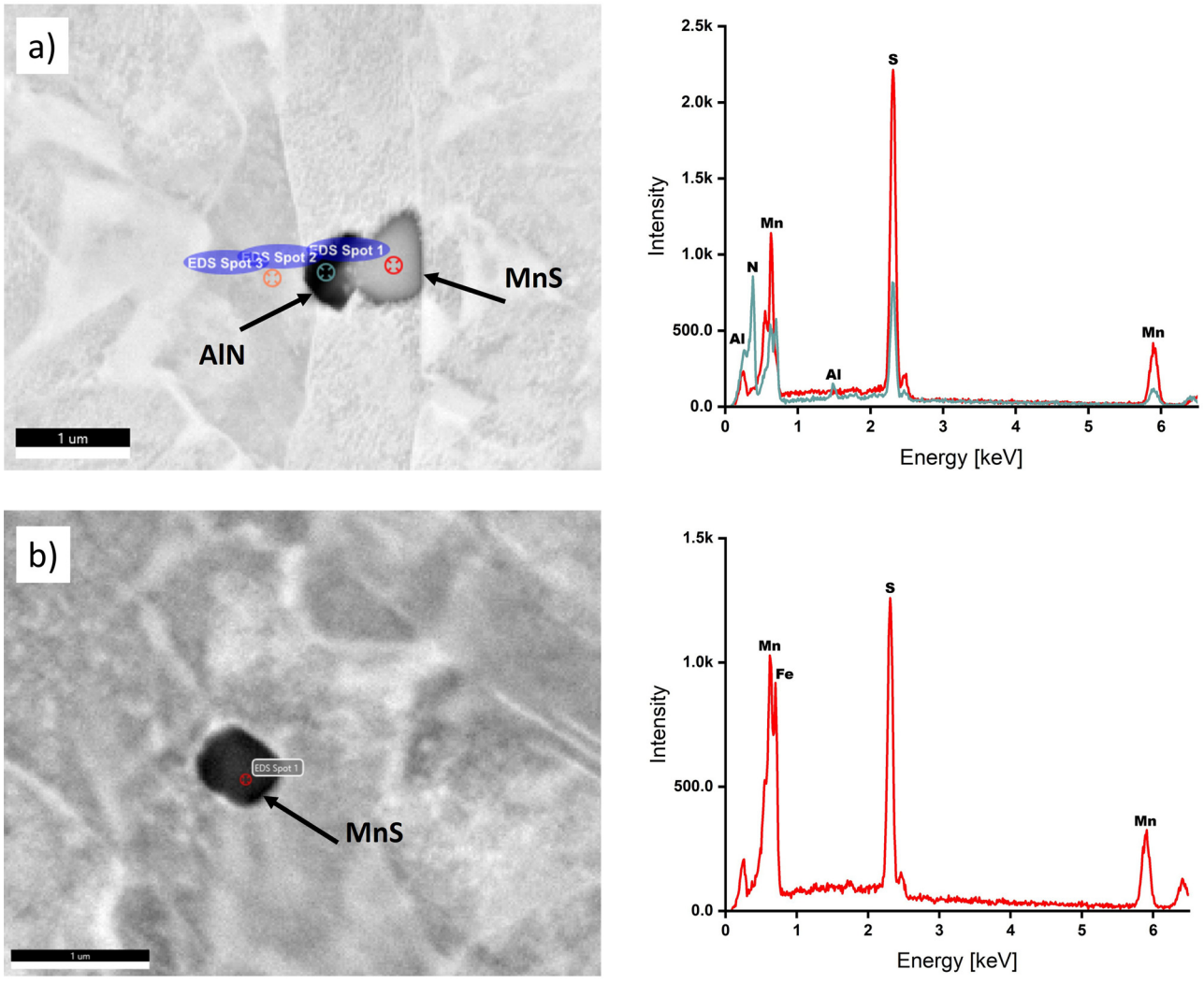

Fig. 7. EDX measurement of precipitates in steel 1: a) AlN at MnS; b) MnS. The scale bar represents 1 µm.

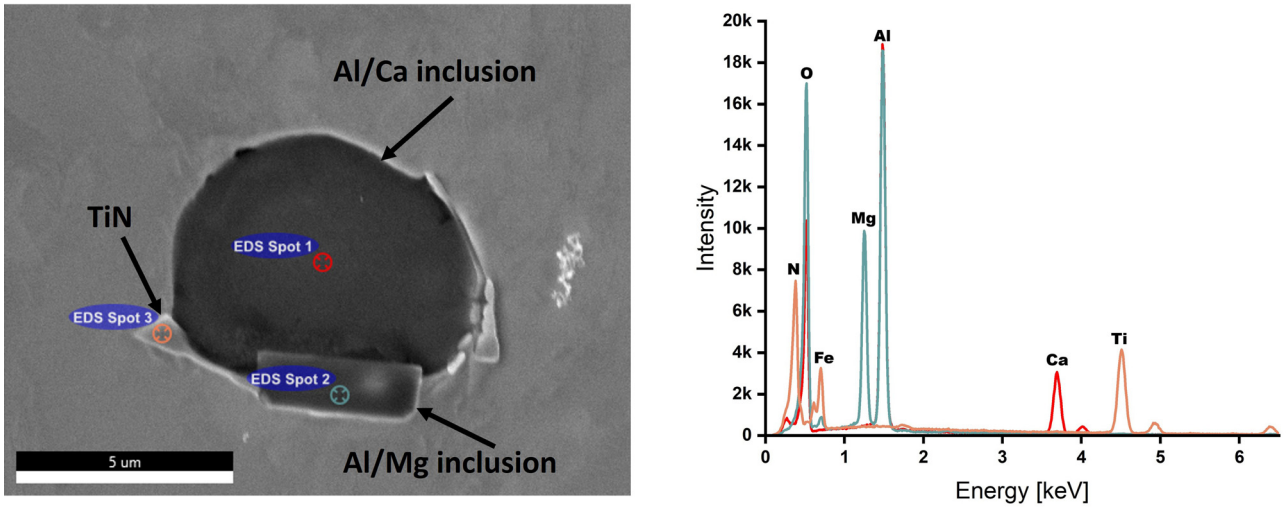

Fig. 8. EDX measurement of Al/Ca and Al/Mg inclusions and TiN precipitates in steel 2. The scale bar represents 5 µm.

formation of detrimental AlN precipitates [8,48,49]. The formation of TiN, AlN, and BN is governed by both thermodynamics and diffusion-controlled kinetics. Wang et al. [50] showed that TiN has a higher starting precipitation temperature compared to BN and AlN, and it starts to precipitate in a solid-liquid state, indicating that TiN was more easily precipitated during solidification, which agrees with MatCalc simulations. In another study [51], it was shown that, despite B having a higher diffusion coefficient than Al and Ti, Ti forms TiN by consuming N at higher temperatures during solidification, suppressing the formation of BN and AlN. Under these conditions, the remaining free B atoms, due to their high mobility, diffuse to austenite grain boundaries and hinder ferrite formation. The MatCalc thermos-kinetic simulation of precipitates, together with the EDX results, confirmed the presence of AlN and MnS in steel 1. These particles increase the susceptibility of the material to crack formation. On the other hand, in steel 2, the formation of coarse TiN precipitates consumes N and retards the formation of AlN and BN, which are detrimental to ductility [52].

5 Conclusion

The hot ductility behavior of the two microalloyed steels was influenced by multiple factors, including thermomechanical conditions, phase transformation, and precipitate behavior.

Chemical composition influences the ductility of the material by varying precipitation kinetics. In this work, steel 2 exhibited better overall ductility than steel 1 under all tested conditions.

The results show that the formation of AlN and MnS promotes crack propagation, whereas the formation of TiN has the opposite effect by consuming N and thereby preventing the formation of AlN. By consuming N, Ti reduces the driving force for fine AlN precipitation that embrittles boundaries. In addition to the influence of Ti on the formation of AlN, steel 2 has lower Al, so less Al is available to form AlN, which also reduces the risk of the formation of AlN at boundaries.

Soluble B tends to segregate to austenite grain boundaries and can strengthen them and retards the formation of intergranular ferrite. Delay of thin ferrite-film formation at boundaries reduces the deformation-induced ferrite, which is the strain localization zone, avoiding intergranular failure. The presence of MnS inclusions in steel 1 contributed to intergranular voiding and further reduced ductility.

For both steels, the size and phase fraction of the precipitates remain nearly constant under various strain rates within the two-phase domain. Therefore, in this region, the ferrite phase governs the ductility behavior of the given material. Thin ferrite films at austenite grain boundaries reduce ductility. The thinner the ferrite film, the more detrimental it is to the ductility. Higher strain rates strengthen ferrite through work hardening and reduce the difference between the strength of ferrite and the strength of austenite, reducing strain concentration in ferrite and improving the ductility. Additionally, during fast deformation, the cracks have less time to propagate and cause further failure. Microstructural analysis confirmed that slower deformation leads to brittle fracture, whereas faster deformation results in mixed ductile-brittle fracture modes. Furthermore, increasing the temperature, within the range of tested temperatures, improves the ductility by reducing the formation of ferrite due to lower undercooling as the driving force for ferrite nucleation.

Acknowledgments

The authors gratefully acknowledge the funding support of K1-MET GmbH, metallurgical competence center. The current research program K1-MET is financed within the Austrian Competence Center program COMET by the Austrian Federal Ministries BMIMI, BMWET, the Federal States of Upper Austria, Styria and Tyrol as well as the SFG and the Standortagentur Tyrol. Continuous support is given by the Upper Austrian Research GmbH. Partial financing is provided by the industrial partner voestalpine Stahl GmbH and the scientific partner Graz University of Technology. Additionally, the authors would like to extend their gratitude to Dr. techn. Fernando Gustavo Warchomicka and Ing. Renáta Palupčíková for their assistance with SEM imaging.

Funding

Austrian funded COMET program (Competence Center Program) K1-MET, funding contract no. FO999892415.

Conflicts of interest

The authors have nothing to disclose.

Data availability statement

The original contributions presented in the study are included in the article, further inquiries can be directed at the corresponding author.

Author contribution statement

Conceptualization, S.B., S.SH, and C.S.; Methodology, S.B. and C.S.; Formal analysis, S.B., S.SH, and C.S.; Investigation, S.B., I. S.; Resources S.I and C.S.; Data curation, S.B.; Writing—original draft preparation, S.B. and S.SH.; Writing—review and editing S. B., S.SH., I.S., S.I., and C.S.; Visualization, S.B; Supervision C.S.; Project administration S.B, S.I., and C.S.; Funding acquisition S. I. and C.S. All authors have read and agreed to the published version of the manuscript.

Supplementary material

Figure S1. Graphical illustrations of the MatCalc simulations from Table 2 and Table 3.

The Supplementary Material is available at https://www.metal-journal.org/10.1051/metal/2026009/olm.

References

1. World Steel Assoc. https://worldsteel.org/data/world-steel-in-figures/world-steel-in-figures-2024/ (2024)

2. X. Jiang, X.M. Cheng, S.H. Song et al., Phosphorus-induced hot ductility enhancement of 1Cr-0.5Mo low alloy steel, Mater. Sci. and Eng. A **574**, 46 (2013)
3. W. Lankford, Some considerations of strength and ductility in the continuous-casting process, Met. Soci. AIME. Metal. Trans. **3**, 1331 (1972)
4. J.K. Brimacombe, K. Sorimachi, Crack formation in the continuous casting of Steel, Metal. Trans. B **8**, 489 (1977)
5. B. Mintz, S. Yue, J. Jonas, Hot ductility of steels and its relationship to the problem of transverse cracking during continuous casting, Intern. Mater. Rev. **36**, 187 (1991)
6. M. Schöbel, S. Großeiber, J. Jonke et al., Residual stresses in continuously cast Steel Slabs, BHM Berg- Und Hütt. Mon. **158**, 475 (2013)
7. B. Mintz, Importance of Ar_3 temperature in controlling ductility and width of hot ductility trough in steels, and its relationship to transverse cracking, Mater. Sci. Techn. **12**, 132 (1996)
8. B. Mintz, The influence of composition on the hot ductility of steels and to the problem of transverse cracking, ISIJ Inter. **39**, 833 (1999)
9. Y. Wang, Q. Ren, L. Zhang et al., Formation and control of transverse corner cracks in the continuous casting slab of a microalloyed steel, St. Res. Int. **92**, (2021)
10. L.H. Chown, L.A. Cornish, Investigation of hot ductility in Al-killed boron steels, Mater. Sci. and Eng. A **494**, 263 (2008)
11. R. Abushosha, S. Ayyad, B. Mintz, Influence of cooling rate and MnS inclusions on hot ductility of steels, Mater. Sci. Techn. **14**, 227 (1998)
12. F. Zarandi, S. Yue, Effect of boron on hot ductility of Nb-microalloyed steels, ISIJ Inter. **46**, 591 (2006)
13. S. Bakhtiari, S.S. Sharifi, S. Ilie et al., Investigation of hot ductility behavior of micro-alloyed steel and the effect of strain rate and dynamic phase transformation on the 2nd ductility minimum, Mater. Wiss. Werkst. Tech. **56**, (2025)
14. A. Cowley, R. Abushosha, B. Mintz, Influence of Ar_3 and Ae_3 temperatures on hot ductility of steels, Mater. Sci. Techn. **14**, 1145 (1998)
15. B. Mintz, R. Abushosha, A. Cowley, Preliminary analysis of hot ductility curve in simple C-Mn steels, Mater. Sci. Techn. **14**, 222 (1998)
16. J. Lewis, J. Jonas, B. Mintz, The formation of deformation induced ferrite during mechanical testing, ISIJ Intern. **38**, 300 (1998)
17. B. Mintz, J.M. Arrowsmith, Hot-ductility behavior of C-Mn-Nb-AI steels and its relationship to crack propagation during the straightening of continuously cast strand, Met. Tech. **24** (1979)
18. F.J. Ma, G.H. Wen, P. Tang et al., Causes of transverse corner cracks in microalloyed steel in vertical bending continuous slab casters, Ironmak. and Steelmak. **37**, 73 (2010)
19. K.M. Banks, A.S. Tuling, B. Mintz, Improved simulation of continuous casting to predict transverse corner cracking in microalloyed Steels, Int. J. Metall. Mater. Eng. **2**, 188 (2013)
20. D.N. Crowther, Z. Mohamed, B. Mintz, The relative influence of dynamic and static precipitation on the hot ductility of microalloyed Steels, Metal. Trans. A **18**, 1929 (1987)
21. N. Wolanska, A.K. Lis, J. Lis, Microstructure investigation of low carbon steel after hot deformation, Jour. of Achi. in Mater. and Manu. Eng. **20**, 291 (2007)
22. Y.L. Gao, X.X. Xue, H. Yang, Influence of boron on initial austenite grain size and hot deformation behavior of boron microalloyed steels, Crys. (Basel). **5**, 592 (2015)
23. R. Abushosha, O. Comineli, B. Mintz, Influence of Ti on hot ductility of C-Mn-Al steels, Mater. Sci. Techn. **15**, 278 (1999)
24. N.E. Hannerz, Critical hot plasticity and transverse slab casting with particular reference cracking in continuous to composition, Trans. ISIJ. **25**, 149 (1985)
25. H. Luo, P. Karjalainen, D. A. Porter et al., The influence of Ti on the hot ductility of Nb-bearing steels in simulated continuous casting process, ISIJ Inter. **42**, 273 (2002)
26. O. Comineli, R. Abushosha, B. Mintz, Influence of titanium and nitrogen on hot ductility of C-Mn-Nb-Al steels, Mater. Sci. Techn. **15**, 1058 (1999)
27. G. Qian, G. Cheng, Z. Hou, The influence of the induced ferrite and precipitates of Ti-bearing steel on the ductility of continuous casting slab, High Temp. Mater. and Proc. **34**, 611 (2015)
28. S.E. Kang, J.R. Banerjee, E.M. Maina et al., Influence of B and Ti on hot ductility of high Al and high Al, Nb containing TWIP steels, Mater. Sci. Techn. (United Kingdom). **29**, 1225 (2013)
29. S.E. Kang, J.R. Banerjee, A.S. Tuling et al., Influence of B on hot ductility of high Al, TWIP steels, Mater. Sci. Techn. (United Kingdom). **30**, 486 (2014)
30. K.C. Cho, D.J. Mun, J.Y. Kim et al., Effect of boron precipitation behavior on the hot ductility of boron containing steel, Metall. Mater. Trans. A Phys. Metall. Mater. Sci. **41**, 1421 (2010)
31. K.C. Cho, D.J. Mun, M.H. Kang et al., Effect of thermal cycle and N content on boron bearing steel, ISIJ Inter. **50**, 839 (2010)
32. W.J. Liu, J. Li, C.B. Shi et al., Effect of boron and titanium addition on the hot ductility of low-carbon Nb-containing Steel, High Temp. Mater. and Proc. **34**, 813 (2015)
33. E. López-Chipres, I. Mejía, C. Maldonado et al., Hot ductility behavior of boron microalloyed steels, Mater. Sci. and Eng. A **464**, 460–461 (2007)
34. S.E. Kang, J.R. Banerjee, A. Tuling et al., Influence of P and N on hot ductility of high Al, boron containing TWIP steels, Mater. Sci. Techn. (United Kingdom). **30**, 1328 (2014)
35. K.M. Banks, A. Tuling, B. Mintz, Influence of thermal history on hot ductility of steel and its relationship to the problem of cracking in continuous casting, Mater. Sci. Techn. **28**, 536 (2012)
36. Y. Maehara, K. Nakai, K. Yasumoto et al., Hot cracking of low alloy steels in simulated continuous casting-direct rolling process, Trans. ISIJ. **28**, 1021 (1987)
37. M. Gontijo, C. Hoflehner, P. Estermann et al., Effect of strain rate on the hot ductility behavior of a continuously cast Ti–Nb microalloyed steel, St. Res. Int. **91**, (2020)
38. Y. Liu, L.X. Du, H.Y. Wu et al., Hot ductility and fracture phenomena of low-carbon V–N–Cr microalloyed steels St. Res. Int. **91**, (2020)
39. B. Mintz, J.R. Banerjee, Influence of C and Mn on hot ductility behavior of steel and its relationship to transverse cracking in continuous casting, Mater. Sci. Techn. **26**, 547 (2010)
40. B. Mintz, Z. Mohamed, Influence of manganese and sulphur on hot ductility of steels heated directly to ten1perature, Mater. Sci. Techn. **5**, 1212 (1989)

41. M. Lückl, T. Wojcik, E. Povoden-Karadeniz et al., Co-Precipitation behavior of MnS and AlN in a Low-Carbon Steel, St. Res. Int. **89** (2018)
42. M. Gontijo, C. Hoflehner, S. Ilie et al., Holding time influence on the hot ductility behavior of a continuously cast low alloy steel, Met. (Basel). **11** (2021)
43. B. Mintz, J.J. Jonas, Influence of strain rate on production of deformation induced ferrite and hot ductility of steels, Mater. Sci. Techn. **10**, 721 (1994)
44. É. Dénes, A.L. Tóth, E.R. Fábián, Qualitative and quantitative analysis of boron content precipitates by FEG-SEM and EDS methods, Mater. Sci. For., **659**, 295 (2010)
45. B. Mintz, D.N. Crowther, Hot ductility of steels and its relationship to the problem of transverse cracking in continuous casting, Intern. Mater. Rev. **55**, 168 (2010)
46. S.S. Sharifi, S. Bakhtiari, E. Shahryari et al., The influence of thermomechanical conditions on the hot ductility of continuously cast microalloyed Steels. Mater. **17**, (2024)
47. S.K. Kim, J. Sung Kim, N.J. Kim, Effect of boron on the hot ductility of Nb-containing steel, Metal. and Mater. Trans. A **33**, 701 (2002)
48. T.N. Baker, Microalloyed steels, Sci. Prog. Oxf. **65**, 493 (1978)
49. T.N. Baker, Microalloyed steels, Ironmak. Steelmak. **43**, 264 (2016)
50. W.S. Wang, H.Y. Zhu, J. Sun et al., Thermodynamic analysis of BN, AlN and TiN precipitation in boron-bearing steel, Metall. **58**, 199 (2019)
51. Y.N. Wang, Y.P. Bao, M. Wang et al., Basic research on precipitation and control of BN inclusions in steel, Metall. Mater. Trans. B **44**, 1144 (2013)
52. M. Gontijo, A. Chakraborty, R.F. Webster et al., Thermomechanical and microstructural analysis of the influence of B- and Ti-content on the hot ductility behavior of microalloyed Steels, Met. (Basel). **12**, 1808 (2022)

Cite this article as: Saeid Bakhtiari, Saham S. Sharifi, Iman Sedighi, Sergiu Ilie, Christof Sommitsch, Influence of alloying elements and strain rate on the second ductility minimum of microalloyed steels during simulated continuous casting, Metall. Res. Technol. **123**, 216 (2026), https://doi.org/10.1051/metal/2026009